



**HAL**  
open science

# Optimization of a dynamic absorber with nonlinear stiffness and damping for the vibration control of a floating offshore wind turbine toy model

Pierre-Olivier Mattei, Renaud Côte

► **To cite this version:**

Pierre-Olivier Mattei, Renaud Côte. Optimization of a dynamic absorber with nonlinear stiffness and damping for the vibration control of a floating offshore wind turbine toy model. *Journal of Theoretical, Computational and Applied Mechanics*, 2023, pp.1-21. 10.46298/jtcam.10123 . hal-03792459v3

**HAL Id: hal-03792459**

**<https://hal.science/hal-03792459v3>**

Submitted on 12 May 2023

**HAL** is a multi-disciplinary open access archive for the deposit and dissemination of scientific research documents, whether they are published or not. The documents may come from teaching and research institutions in France or abroad, or from public or private research centers.

L'archive ouverte pluridisciplinaire **HAL**, est destinée au dépôt et à la diffusion de documents scientifiques de niveau recherche, publiés ou non, émanant des établissements d'enseignement et de recherche français ou étrangers, des laboratoires publics ou privés.

## Identifiers

DOI 10.46298/jtcam.10123

HAL hal-03792459v3

## History

Received Oct 22, 2022

Accepted Feb 28, 2023

Published May 12, 2023

## Associate Editor

Olivier THOMAS

## Reviewers

Anonymous

Kevin DEKEMELE

Sébastien SEGUY

## Open Review

OAI hal-04082019

## Licence

CC BY 4.0

©The Authors

# Optimization of a dynamic absorber with nonlinear stiffness and damping for the vibration control of a floating offshore wind turbine toy model

✉ Pierre-Olivier MATTEI and ✉ Renaud CÔTE

Aix Marseille Université, CNRS, Centrale Marseille, LMA UMR 7031, 4 impasse Nikola Tesla, Marseille, France

Passive vibration mitigation of offshore wind turbines using nonlinear absorbers or nonlinear energy sinks has begun to receive attention in the literature. In most cases, little attention has been paid to the possibility of detached resonances that occur when a nonlinear energy sink is attached to the linear system describing the wind turbine. Sea motions that alter the initial conditions of the floating offshore wind turbine may cause the nonlinear energy sink to operate at one or more detached resonances, completely negating its ability to control turbine vibration. In this paper, we are interested in optimizing the parameters of a nonlinear energy sink with nonlinear stiffness and nonlinear viscous damping for vibration control of a toy model (e.g., a linear mass-spring-damper system) of a floating offshore wind turbine over its entire operating range. The mechanism of detached resonance cancellation is studied analytically under the 1:1 resonance. It is shown that nonlinear energy reduction with properly tuned nonlinear viscous damping allows the complete elimination of undesired regimes and fully restores the absorber's ability to strongly limit the vibration of a floating offshore wind turbine over its entire forcing range. The results obtained over a wide range of parameters suggest that both the optimal nonlinear energy sink parameters (linear and nonlinear stiffness and nonlinear damping) and the damping of the vibration of a floating offshore wind turbine depend on simple power laws of the nonlinear energy sink mass and linear damping.

**Keywords:** passive vibration reduction, nonlinear energy sink, geometrically nonlinear damping, floating offshore wind turbine.

## 1 Introduction

Renewable wind energy is developing rapidly these days. Offshore wind turbines are particularly suited to generating high power in different environmental conditions. In fact, they are subject to more regular wind conditions than on land, and it is possible to develop large wind turbines that are more energy efficient, with slender towers and extremely long blades, and less disruptive to local residents and wildlife. Among these, Floating Offshore Wind Turbines (FOWT) are easy to implement in deep water farms and are likely to develop strongly in the coming years. This type of wind turbine is gigantic in size (with a height of almost 100 m and 150 m with the blades), very heavy (with a mass of almost 1000 tonnes) and has dynamic characteristics that are difficult to control. Most wind turbine primary resonances are below 1 Hz (typically 0.3 Hz to 0.5 Hz) and have very low intrinsic damping. FOWTs are subjected to various types of dynamic loads such as environmental loads (wave and wind), aero-structure interaction loads and mechanical loads (inertial and controller effects). These loads induce vibrations in the wind turbine tower, which are transmitted to the floating foundation and mooring lines, increasing the overall ultimate loads and fatigue cycles.

Mitigating the vibration of wind turbines (WT) under dynamic loads such as wind, sea waves and earthquakes has been addressed by many researchers (see Zuo et al. 2020). Since no external energy is required, most studies have been conducted on passive linear devices, such as single (TMD) or multiple tuned mass dampers (MTMD) or tuned liquid dampers (TLD), thanks to their ability to improve the damping of the whole system. Classically, a TMD is optimized near a

Acronyms			
[F](O)WT	[Floating] (Offshore) Wind Turbines	MTMD	Multiple Tuned Mass Damper
CX-A	Manevitch Complexification-Averaging	NES	Nonlinear Energy Sink
EMD	Empirical Mode Decomposition	RMS	Root Mean Square
FRF	Frequency Response Function	SIM	Slow Invariant Manifold
HHT	Hilbert-Huang Transform	SMR	Strongly Modulated Response
HSA	Hilbert Spectral Analysis	TLD	Tuned Liquid Damper
IMF	Intrinsic Mode Function	TMD	Tuned Mass Damper

specific frequency of the WT to be controlled and is effective in a narrow frequency band. Slight frequency detuning between the TMD and the controlled structure can significantly change the efficiency of the TMD. FOWTs are often located in harsh marine environments and their natural resonances are altered not only by design and construction discrepancies, but also by operating conditions, degradation of material properties or structural damage.

Since the first seminal work by Gendelman et al. (2001), the nonlinear passive dynamic absorber, also known as the nonlinear energy sink (NES), which can be seen as an extension of Den Hartog's TMD to correct its lack of robustness to variation in the primary system, has received increasing attention from academia and industry (Ding and Chen 2020). NES typically consists of a small mass, a viscous damper and a pure nonlinear stiffness element. The essentially nonlinear stiffness allows system dynamics without a fixed frequency, resulting in a wide frequency band capability in dissipating energy from the host structure. Therefore, NESs are robust to any structural frequency changes. As shown by Gendelman et al. (2001), a restoring force of a third order power of deformation causes the vibrational energy of the controlled structure to be irreversibly transferred to a cubic NES. Since then, many kinds of NESs have been designed, such as serial cubic NES (Gendelman et al. 2011), bistable NES (AL-Shudeifat 2014), magnet-based NES (Chen et al. 2020), vibro-impact NES (Gourc et al. 2015), or track NES which provide a nonlinear restoring force similar to that of a cubic NES (Wang et al. 2015) to improve their efficiency. A particular track NES, which provides a nonlinear restoring force similar to that of a bistable-like NES, has recently been used by Zuo and Zhu (2022) to control earthquake-induced vibrations in OWTs.

One of the main difficulties in using a NES to damp oscillatory motion is that, under periodic forcing, there is a high amplitude detached resonance solution in the frequency response function (FRF) of nonlinear oscillatory systems which must be avoided at all costs. The occurrence of such detached resonances in nonlinear oscillators has long been known (Rauscher 1938; Abramson 1955). The nonlinearity could be that of the elastic restoring force (Alexander and Schilder 2009) or that of the damping force (Habib et al. 2018). To overcome this difficulty, the parameters of the NES must be constrained to a certain range of spatial parameters (Gourc et al. 2014). Although efficient, this procedure limits the ability to maximize the attenuation obtained by the NES.

The most interesting way to overcome such detached resonance is to use tuned nonlinear damping. As shown by Starosvetsky and Gendelman (2009), who use a quadratic damping whose characteristics are composed of two parts: a low and a high amplitude quadratic damping, which differ only in their coefficients: damping force  $f = \lambda_1 \dot{x}|\dot{x}|$ ,  $x < x_{cr}$  and  $f = \lambda_2 \dot{x}|\dot{x}|$ ,  $x > x_{cr}$ . Using Manevitch's complexification averaging (CX-A) under the 1:1 resonance, the authors compute the slow invariant manifold (SIM) of the system, which allows to analyze the strongly modulated response (SMR), which is the best way to dissipate energy in such a system; they observe that the destruction of the detached resonance is achieved when the high amplitude quadratic damping coefficient  $\lambda_2$  is sufficiently larger than  $\lambda_1$ , they gave a ratio of 12 in their example. The problem pointed out by the authors is that the optimization procedure fails when the upper detached resonance merges with the lower branch main resonance curve. It is worth noting that the main resonance curve can be viewed as the FRF of a normal linear system. Similarly, viscous nonlinear damping has been studied by Andersen et al. (2012), who define a NES consisting of a mass attached to two additional elements composed of inclined parallel linear spring-damper pairs. The transverse motion of the mass induces not only linear and cubic stiffness (which is the usual way to construct nonlinear springs and NES), but also linear and cubic viscous damping. In their work, the authors had found that the presence of nonlinear damping can cause the structure to exhibit dynamic instabilities.

This type of nonlinear damping is analogous to that observed by Bellet et al. (2010) when applying the concept of targeted energy transfer to the field of acoustics, using a high amplitude vibrating membrane as a NES. It was also used by Liu et al. (2019), who generalized NES by allowing inclined parallel linear spring-damper pairs to form an initial angle  $\phi_0$  at rest. This not only allows for high amplitude transverse motion, but also allows the dynamics of the system to be either stiffened or softened at different phases of motion, depending on the initial angle of inclination. In this work, the authors observed that by using appropriate values for the NES parameters, unwanted detached resonances can be completely eliminated.

The NES model proposed by Andersen et al. (2012) underpins the work presented below.

Only air-structure interaction loads are considered in this paper. FOWTs operate over a wide range of wind speeds (typically between 5 and 40 knots) and their operating principle is that the blade speed is essentially constant. In practice, as shown by Pahn et al. (2012) in real cases, the tower of a wind turbine is subjected to a thrust force composed of an almost constant term and a periodic force  $F(t) = A_0 + A \cos \omega t$  with  $\omega = 2\pi f$  where  $f$  is the force frequency, which depends mainly on the wind speed variations, the rotation speed and the number of blades of the FOWT. In the various cases considered in this work, most of the dynamic components are below 1 Hz with a maximum amplitude of about 10 kN. In the following, the constant term  $A_0$  is neglected.

To simplify calculations, the wind turbine is described as a linear mass-spring-damper system coupled to a NES with linear and cubic stiffness and damping characteristics.

In this paper, we are interested in optimizing the parameters (linear and nonlinear stiffness and nonlinear damping) of the NES for vibration control of the suggested toy model over its entire operating range under periodic forcing. To this end, a two-step procedure is proposed. During the first pass, the occurrence of detached resonances is limited by imposing a zero initial condition and, for a set of fixed NES mass and linear damping, the linear and nonlinear stiffness of the NES are optimized to reduce the vibration of the FOWT over its entire forcing range. Once the optimal parameters have been determined, non-zero initial conditions are imposed to exhibit detached resonances and the nonlinear damping is adjusted to cancel them out. Results obtained over a wide range of parameters suggest that both the optimal NES parameters (linear and nonlinear stiffness and nonlinear damping) and the attenuation of FOWT vibration depend regularly on NES mass and linear damping.

The paper is structured as follows. The second section is dedicated to the description of the problem. The third section is dedicated to the presentation of the numerical method that solves the exact equations and to the introduction of the optimization from two aspects, first by using literature results that avoid the problem of detached resonances, and second by showing how the optimal vibration reduction obtained by using brute force without considering detached resonances is completely wiped out when they occur. The fourth section is devoted to an analytical study of nonlinear damping to show that, when used to control detached resonances, it does not alter the underlying mechanism of energy transfer. The cancellation of detached resonances is studied analytically under the 1:1 resonance. It is shown that the NES, with properly tuned nonlinear viscous damping, allows the complete elimination of undesired regimes and fully restores the absorber's ability to strongly limit FOWT vibration over its entire forcing range. To ensure that this nonlinear damping does not alter the dynamics of the system too much, the slow flow of the system is studied by calculating its slow invariant manifold. It is shown that, although not perfectly describing all the features of the exact solution, most of the characteristics of the slow flow are preserved when the nonlinear damping is taken into account. The fifth section is devoted to a synthetic presentation of the optimization results obtained using brute force and detached resonance cancellation; it is shown that the linear, nonlinear stiffness and nonlinear damping of the NES and the attenuation of the FOWT vibrational motion depend on simple power laws of the NES mass and linear damping. The sixth section is devoted to the conclusion.

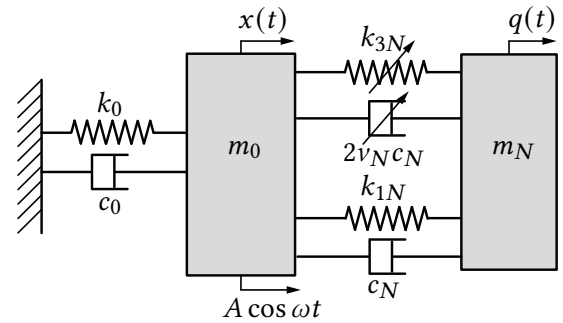
## 2 Equations of the problem

The considered wind turbine has a resonant frequency of 0.5 Hz and a damping  $\zeta_0$  of 0.05 %. The forcing frequency  $f$  varies over a third of an octave around 0.5 Hz (close to the wind turbine resonance) and the force applied to the wind turbine tower  $A$  varies between  $A_{\min} = 3$  N and

$A_{\max} = 10$  kN; the minimum value of 3 N was chosen as a compromise between a maximum amplitude to ensure linear motion for the NES and a minimum amplitude to ensure numerically regular computation for the main system (a too small forcing amplitude leads to numerical instabilities).

Figure 1 shows a simplified and idealized nonlinear system describing the FOWT together with the NES. A primary mass  $m_0$  is attached to the ground by a linear spring  $k_0$  and a viscous damper  $c_0$ . It is excited by a harmonic force  $A \cos \omega t$ . The NES connected to the primary mass consists of an oscillator of mass  $m_N$  with a linear spring  $k_{1N}$  and a linear viscous damper  $c_{1N}$  along with a nonlinear spring  $k_{3N}$  and a nonlinear viscous damper  $2v_N c_N$ , all NES parameters being independent.

**Figure 1** Model of a simplified two-degree-of-freedom FOWT/NES system.



Let  $x(t)$  be the displacement of the linear system and  $q(t)$  the displacement of the NES with  $w(t) = x(t) - q(t)$ . With the classical convention  $\dot{x}(t) = dx(t)/dt$ , the dynamics of the two-degree-of-freedom system reads

$$m_0 \ddot{x}(t) + c_0 \dot{x}(t) + k_0 x(t) + c_N (1 + 2v_N w^2(t)) \dot{w}(t) + k_{1N} w(t) + k_{3N} w(t)^3 = A \cos \omega t \quad (1a)$$

$$m_N \ddot{q}(t) - c_N (1 + 2v_N w^2(t)) \dot{w}(t) - k_{1N} w(t) - k_{3N} w(t)^3 = 0 \quad (1b)$$

where  $m_0 = 10^6$  kg is the weight of the FOWT and  $k_0 \approx 10^7$  N/m is its stiffness, yielding a pulsation  $\omega_0 = \sqrt{10} \approx \pi$ . A damping coefficient  $\zeta_0 = 0.05\%$  gives a viscosity  $c_0 = 2\zeta_0 m_0 \omega_0 \approx 3,200$  N s/m. The mass of the NES is  $m_N$ , its linear stiffness,  $k_{1N}$ , its cubic stiffness,  $k_{3N}$  and its linear viscosity coefficient,  $c_N$ . The nonlinear viscous damping  $(1 + 2v_N w^2(t)) \dot{w}(t)$  is derived from (Andersen et al. 2012);  $c_N v_N$  is the nonlinear viscous damping coefficient. Equation (1) comes with the initial conditions  $x(0) = x_0$ ,  $\dot{x}(0) = \dot{x}_0$  and  $q(0) = q_0$ ,  $\dot{q}(0) = \dot{q}_0$ .

The corresponding non-dimensional parameters are  $\Omega = \omega/\omega_0$ ,  $\tau = \omega_0 t$ ,  $\epsilon = m_N/m_0$ ,  $\lambda_0 = c_0/(m_N \omega_0)$ ,  $\lambda_N = c_N/(m_N \omega_0) = \mu_N \lambda_0$ ,  $\delta_N = k_{1N}/(m_N \omega_0^2)$ ,  $K_N = k_{3N}/(m_N \omega_0^2)$  and  $F = A/(m_N \omega_0^2)$ . Equation (1) becomes

$$\ddot{x}(\tau) + \epsilon \lambda_0 \dot{x}(\tau) + x(\tau) + \epsilon \mu_N \lambda_0 (1 + 2v_N w^2(\tau)) \dot{w}(\tau) + \epsilon \delta_N w(\tau) + \epsilon K_N w(\tau)^3 = \epsilon F \cos \Omega \tau \quad (2a)$$

$$\epsilon \ddot{q}(\tau) - \epsilon \mu_N \lambda_0 (1 + 2v_N w^2(\tau)) \dot{w}(\tau) - \epsilon \delta_N w(\tau) - \epsilon K_N w(\tau)^3 = 0 \quad (2b)$$

The solution can be calculated numerically without difficulty. For example, on a laptop workstation, using Mathematica's NSolve function (Wolfram Research, Inc. 2021) takes a fraction of a second for each amplitude-frequency pair for a calculation over a forcing period of more than an hour.

### 3 Parameter optimization of the exact equations

#### 3.1 Optimization using literature rules

A first optimization, considering only the linear damping component, was performed using literature rules, such as the one proposed for  $K_N$  by Starosvetsky and Gendelman (2008). The chosen parameters, which avoid the problem of detached resonance by the procedure described in Gourc et al. (2014), were set to  $\epsilon = 0.01$ ,  $\lambda_0 = 0.1$ ,  $\mu_N = 2$ ,  $\delta_N = 0.03$  and  $K_N = 28$ . The FRF covering 1/6 of an octave on either side of the wind turbine resonance is shown in Figure 2. In this figure,  $L(A, f) = x_{\text{rms}}(A, f)/A$ , where  $x_{\text{rms}}(A, f)$  is the root mean square (RMS) of the steady state FOWT amplitude for a given amplitude  $A$  and forcing frequency  $f$ , and  $x_{\text{rms}}(A, f)$  is

estimated by averaging  $x(\tau)$  over the last half-hour of motion. All calculations to solve the initial system in Equations (2a) and (2b) considered 101 points in frequency and 16 points in amplitude, and each of them requires about one minute of computation using parallel computation on 16 cores of a Dell Poweredge R640 workstation.

In Figure 2 and all subsequent figures, levels are indicated in decibels, calculated as  $20 \log(|L|/L_r)$ , where  $L_r = 1$  is the reference level. Figure 2 [left] corresponds to the surface response over the whole amplitude and frequency range, and the right sub-figure corresponds to the ridge curve with free and blocked NES (to see its efficiency). The ridge curve is obtained by taking, for each amplitude, the maximum frequency response over the considered frequency range. This is needed because, for such a nonlinear system, the maximum frequency of the frequency response varies with the forcing amplitude. Obviously, when the NES is blocked, the maximum amplitude is constant. The ridge curve shows a quasi-linear decrease in amplitude, which is a common effect of NES acting as an amplitude limiter over its efficiency range.

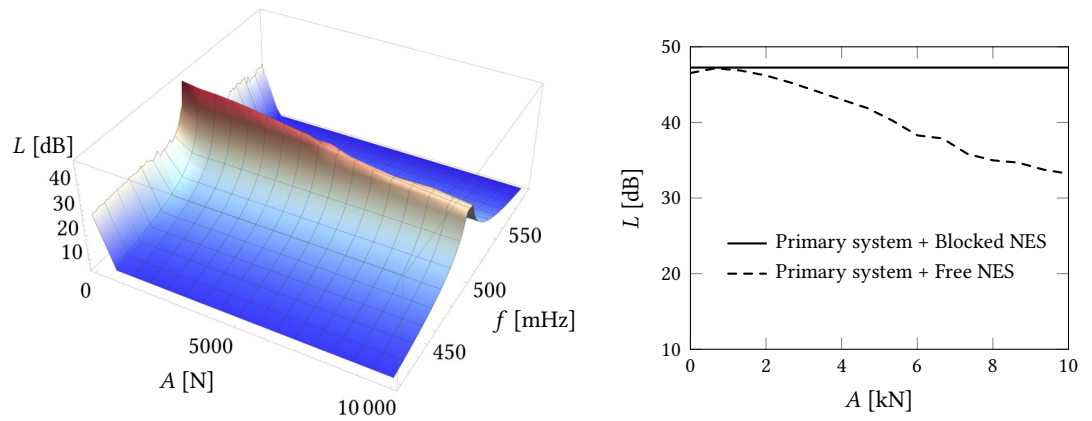


**Figure 2** WT FRF with NES and  $f_0^r = 0.5$  Hz. [Left] 3D surface response. [Right] ridge curve.

These results are compared with those of an optimized TMD with the same mass as the NES to control resonance at 0.5 Hz. Many expressions for the parameters ( $\delta_{\text{TMD}}$  characterizes the linear stiffness and  $\mu_{\text{TMD}}$ , the linear damping) are available in the literature since the pioneering work of Den Hartog (1947). The TMD parameters used, valid for an undamped system, which is almost the case for the FOWT under consideration, are those proposed by Bakre and Jangid (2007):

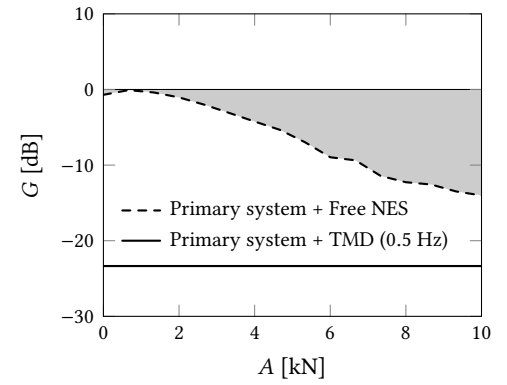
$$\delta_{\text{TMD}} = \frac{2 + \epsilon}{2(1 + \epsilon)^2}, \quad \mu_{\text{TMD}} = \frac{1}{\lambda_0} \sqrt{\frac{\epsilon(3\epsilon + 4)}{8(1 + \epsilon)(2 + \epsilon)}}. \quad (3)$$

The comparison is shown in Figure 3. In this and the following figures, damping is represented as the inverse of the gain  $G(A)$  provided by NES and a TMD: a negative gain indicates a decrease in vibration level and then damping, while a positive value indicates an increase in vibration level. The various gain curves are simply the FOWT ridge curves normalized by their amplitude in decibels at their main resonance, without taking into account nonlinear components for the NES (*i.e.*, a 2-dof damped linear system). For the considered FOWT, the TMD characteristics in Equation (3) are  $\epsilon = 0.01$ , that is  $\delta_{\text{TMD}} = 0.985$  and  $\mu_{\text{TMD}} = 0.498$ . For each amplitude  $A$ , the level of the normalized ridge curve is defined by  $G(A) = \max_f L(A, f) / (A \max_f L_{\text{lin}}(f))$  where  $\max_f L_{\text{lin}}(f)$  is the maximum amplitude of the corresponding linear system obtained by cancelling the nonlinear part of the NES characteristics in Equation (1). The damping allowed by the TMD is calculated in a similar way and remains constant over the entire amplitude range.

In Figure 3, the maximum amplitude of the 2-dof system is reached at the resonant frequency of the FOWT without NES, near 0.5 Hz. However, since  $\delta_N = 0.03$ , the linear resonant frequency of the NES is  $0.5 \times \sqrt{\delta_N} \approx 0.09$  Hz is outside the plotted range.

These results are satisfactory, with a maximum reduction in vibration level  $-20 \log |G|$  of 14 dB and an average of 5.3 dB. The aim of the optimization in the next sections is to achieve a higher reduction. For the current configuration, TMD gives a much better reduction of 23.3 dB, so the aim is to get as close as possible to the TMD result.

**Figure 3** Attenuation (*i.e.* inverse of gain) for NES and TMD optimized for 0.5 Hz resonance.



### 3.2 Brute force optimization: detached resonances

Among the possible functional choices, it was decided to minimize the mean of the  $G(A)$  ridge curve to obtain the highest mean attenuation. This corresponds to the shaded area shown in Figure 3. At this stage, in order to avoid detached resonances, the initial conditions are set to zero for each calculation:  $x_0 = 0$ ,  $\dot{x}_0 = 0$ ,  $q_0 = 0$  and  $\dot{q}_0 = 0$ .

Minimizing only for the highest forcing excitation,  $A_{\max} = 10,000$  N in the present study, would have been too irrelevant, since in many cases, even for zero initial conditions, detached resonances appear around  $A_{\max}$  and transform the minimization process into a non-convergent one. Then the functional  $J$  to be minimized is defined as

$$J = \frac{1}{A_{\max} - A_{\min}} \int_{A_{\min}}^{A_{\max}} G(A) dA \tag{4}$$

Without constraints on the parameters ( $\epsilon$ ,  $\mu_N$ ,  $\delta_N$ ,  $K_N$ ), all optimizations systematically increased the NES mass  $\epsilon$  and decreased its damping  $\mu_N$ . The solution is to fix a pair of parameters  $\epsilon$  and  $\mu_N$  and optimize for each pair  $\delta_n$  and  $K_N$ . Optimizing, for two parameters, in Mathematica (Wolfram Research, Inc. 2021) uses a Nelder-Mead type algorithm and requires between two and three days of parallel computation using 16 cores on a Dell Poweredge R640 workstation.

For example,  $\epsilon = 0.02$  and  $\mu_N = 0.2$  gives the optimal parameters  $\delta_n = 0.5$  and  $K_N = 43$  with an average  $-20 \log |J|$  attenuation of 16.1 dB and a maximum attenuation achieved at  $A = A_{\max}$ ,  $-G(A_{\max}) = 28.1$  dB, compared to the 31 dB attenuation provided by the TMD observed in Figure 4, the TMD characteristics given in Equation (3) for this case are  $\delta_{\text{TMD}} = 0.97$  and  $\mu_{\text{TMD}} = 1.4$ . It is worth noting that a classic result from literature (Habib and Romeo 2020) is recovered, for which TMD and NES, although based on different mechanical properties, have similar performance when the NES is optimized for a given forcing.

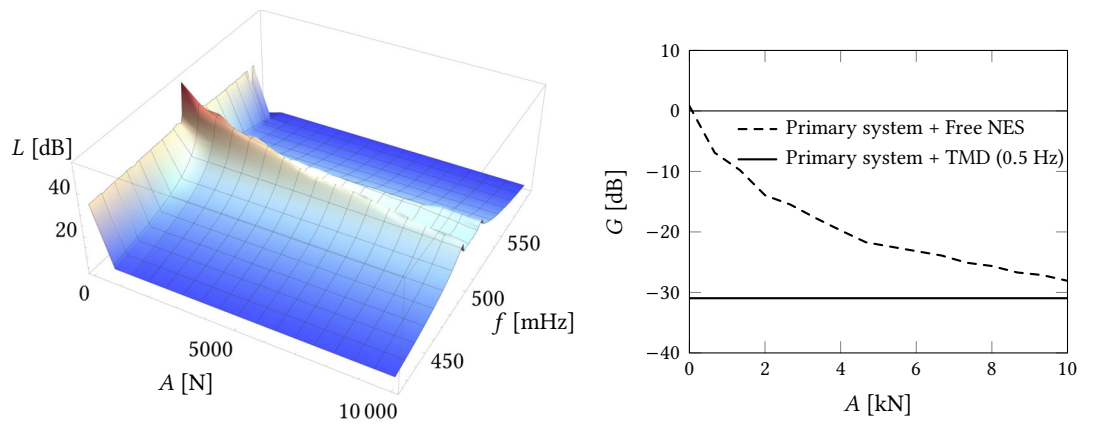


**Figure 4** Optimal attenuation for  $\epsilon = 0.02$  and  $\mu_N = 0.2$ :  $\delta_n = 0.5$  and  $K_N = 43$ .

If the possibility of one or more detached resonances is taken into account by imposing the non-zero initial conditions  $x_0 = 0.1$ ,  $\dot{x}_0 = 0.1$ ,  $q_0 = 0$  and  $\dot{q}_0 = 0$ , results change dramatically as shown in Figure 5. Many high amplitude detached resonances appear and the NES no longer features vibration reduction.

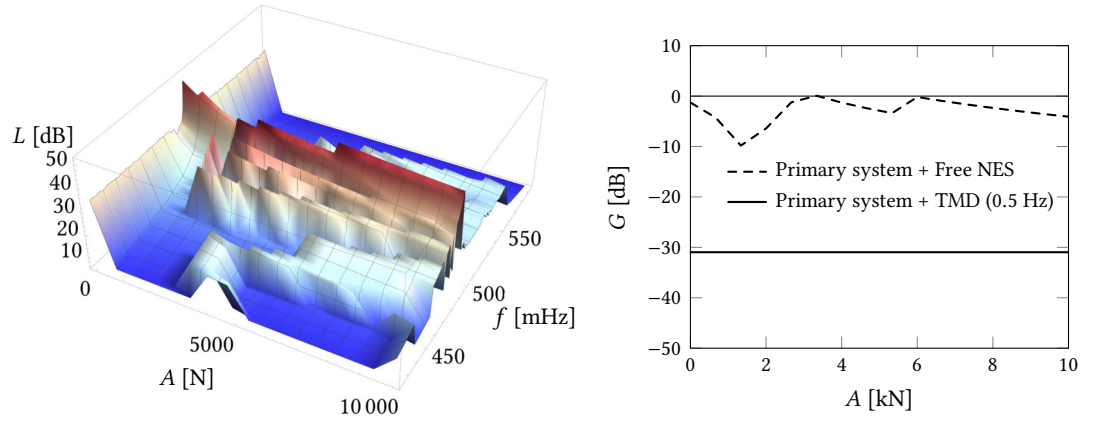


**Figure 5** Attenuation for  $\epsilon = 0.02$  and  $\mu_N = 0.2$ :  $\delta_n = 0.5$  and  $K_N = 43$  with detached resonance.

## 4 Nonlinear damping as a controller of detached resonance: analytical study

Before optimizing the nonlinear damping parameter  $\nu_N$ , it is necessary to check that this type of damping does not change the nature of the solution. To do so, the fixed-points and the SIM of the system are computed, assuming that the motion is under 1:1 resonance.

### 4.1 Fixed-points

Under 1:1 resonance, the CX-A method (Vakakis et al. 2008, Ch. 6) is applied. One starts from Equations (2a) and (2b) in which the change of variable  $v = x + \epsilon q$  is introduced. This results in

$$\ddot{v} + \frac{v + \epsilon w}{1 + \epsilon} + \epsilon \lambda_0 \frac{\dot{v} + \epsilon \dot{w}}{1 + \epsilon} = \epsilon F \cos \Omega \tau \quad (5a)$$

$$\ddot{w} + \frac{v + \epsilon w}{1 + \epsilon} + \epsilon \lambda_0 \frac{\dot{v} + \epsilon \dot{w}}{1 + \epsilon} + (1 + \epsilon)(\delta_N w + \mu_N \lambda_0 (1 + 2\nu_N w^2) \dot{w} + K_N w^3) = \epsilon F \cos \Omega \tau \quad (5b)$$

CX-A introduces the new variables  $\Phi_1 \exp(i\Omega\tau) = \dot{v} + i\Omega v$  and  $\Phi_2 \exp(i\Omega\tau) = \dot{w} + i\Omega w$  to be inserted into Equation (5). Averaging over the frequency  $\Omega$  yields

$$\dot{\Phi}_1 + i\frac{\Omega}{2}\Phi_1 + \frac{\Phi_1 + \epsilon\Phi_2}{2(1 + \epsilon)}\left(\epsilon\lambda_0 - \frac{i}{\Omega}\right) = \epsilon\frac{F}{2} \quad (6a)$$

$$\dot{\Phi}_2 + i\frac{\Omega}{2}\Phi_2 + \frac{\Phi_1 + \epsilon\Phi_2}{2(1 + \epsilon)}\left(\epsilon\lambda_0 - \frac{i}{\Omega}\right) + \frac{(1 + \epsilon)\Phi_2}{2\Omega}\left(-i\delta_N + \mu_N\lambda_0\Omega - \frac{3iK'_N}{2\Omega^2}|\Phi_2|^2\right) = \epsilon\frac{F}{2} \quad (6b)$$

with  $K'_N = K_N(1 - \nu_N\mu_N\lambda_0\frac{2\Omega}{3iK_N})$ . It is easy to see that taking nonlinear damping into account leads to a simple modification of the nonlinear stiffness term in the usual form of an imaginary frequency-dependent term. It is worth noting that this system represents the slow flow of steady-state dynamics under the 1:1-resonance condition.

The fixed-points  $\Phi_{1,2}^0$  are solutions of the slow flow for  $\dot{\Phi}_{1,2} = 0$ , that is:

$$\Phi_1^0 = \frac{i\epsilon\Phi_2^0 + \epsilon F(1 + \epsilon)\Omega - \epsilon^2\lambda_0\Phi_2^0\Omega}{i(\Omega^2 - 1) + \epsilon\Omega(i\Omega + \lambda_0)} \quad (7a)$$

where  $\Phi_2^0$  is solution to

$$1 + c_1\Phi_2^0 + c_2\Phi_2^0|\Phi_2^0|^2 = 0. \quad (7b)$$

The coefficients  $c_1$  and  $c_2$  read

$$c_1 = \frac{-i\delta_N + \lambda_0\Omega(\mu_N + \epsilon\delta_N) + i\Omega^2(1 + (1 + \epsilon)\delta_N - \epsilon\lambda_0^2\mu_N) - \lambda_0\Omega^3(\epsilon + (1 + \epsilon)\mu_N) - i\Omega^4}{F\epsilon\Omega^3} \quad (8a)$$

$$c_2 = \frac{3K'_N(-i + \epsilon\lambda_0\Omega + i(1 + \epsilon)\Omega^2)}{4\epsilon F\Omega^5}. \quad (8b)$$



In order to solve Equation (7b), it is first translated into a polynomial form in  $|\Phi_2^0|^2$

$$1 + a_1|\Phi_2^0|^2 + a_2|\Phi_2^0|^4 + a_3|\Phi_2^0|^6 = 0 \quad (9)$$

where the real coefficients are

$$a_1 = -|c_1|^2 \quad (10a)$$

$$a_2 = -|c_1 + c_2|^2 + |c_1|^2 + |c_2|^2 \quad (10b)$$

$$a_3 = -|c_2|^2. \quad (10c)$$

The polynomial of degree 3 in  $|\Phi_2^0|^2$  in Equation (9) has one or three real roots depending on the system parameters. The stability of these roots is obtained by a usual linearisation of a complex perturbation around the fixed-points. Roughly, it consists of adding small perturbations around the fixed-points, that is  $\Phi_1 = \Phi_1^0 + \rho_1$  and  $\Phi_2 = \Phi_2^0 + \rho_2$ . This change of variables is introduced into the averaged System (6) and linearisation leads to

$$\begin{pmatrix} \dot{\rho}_1 \\ \dot{\rho}_2 \\ \dot{\rho}_1^* \\ \dot{\rho}_2^* \end{pmatrix} = \begin{bmatrix} A_{11} & A_{12} & 0 & 0 \\ A_{21} & A_{22} & 0 & A_{24} \\ 0 & 0 & A_{11}^* & A_{12}^* \\ 0 & A_{24}^* & A_{21}^* & A_{22}^* \end{bmatrix} \begin{pmatrix} \rho_1 \\ \rho_2 \\ \rho_1^* \\ \rho_2^* \end{pmatrix} \quad (11)$$

where  $z^*$  is the complex conjugate of  $z$ . The matrix coefficients read

$$A_{11} = -i\frac{\Omega}{2} - \frac{1}{2(1+\epsilon)}\left(\epsilon\lambda_0 - \frac{i}{\Omega}\right) \quad (12a)$$

$$A_{12} = \epsilon A_{21} \quad (12b)$$

$$A_{21} = -\frac{1}{2(1+\epsilon)}\left(\epsilon\lambda_0 - \frac{i}{\Omega}\right) \quad (12c)$$

$$A_{22} = -i\frac{\Omega}{2} - \frac{\epsilon}{2(1+\epsilon)}\left(\epsilon\lambda_0 - \frac{i}{\Omega}\right) + i\delta_N\frac{1+\epsilon}{2\Omega} - \mu_N\lambda_0\frac{1+\epsilon}{2} + \frac{3iK'_N}{4\Omega^3}(1+\epsilon)|\Phi_2^0|^2 \quad (12d)$$

$$A_{24} = \frac{3iK'_N}{8\Omega^3}(1+\epsilon)\Phi_2^0 \quad (12e)$$

The stability of a fixed-point is determined by calculating the roots of the characteristic polynomial of the system matrix given in Equation (11). If all roots have a negative real part, then the fixed-point is stable. If a real root crosses the half-complex plane, the fixed-point is a saddle-node. If a pair of complex roots leaves the left part of the complex plane, there is a slow-flow Hopf bifurcation.

Once the amplitude  $|\Phi_2^0|$  has been calculated, by writing  $\Phi_2^0 = |\Phi_2^0| \exp(i\theta)$ , it is easy to show that the phase  $\theta$  is given by  $\theta = \pi - i \ln(c_1|\Phi_2^0| + c_2|\Phi_2^0|^3)$ . Then,  $\Phi_1^0$  is calculated by solving Equation (7a) for each value of  $\Phi_2^0$ .

By introducing a detuning parameter  $\sigma$  such that  $\Omega = 1 + \epsilon\sigma$ , for  $A = 10,000$  N,  $\epsilon = 0.02$ ,  $\mu_N = 0.2$ ,  $\delta_N = 0.5$  and  $K_N = 43$ , it is easy to obtain the stable fixed-points of the primary system displacement normalized by forcing  $|x^0|/F$ , with and without nonlinear damping. The results are presented in Figure 6:  $|x^0|/F = |(\Phi_1^0 + \epsilon\Phi_2^0)/(1+\epsilon)^2|/F$ . In this figure, the centre frequency obtained for  $\sigma = 0$  is  $f_0 = \frac{\omega_0}{2\pi} \approx 0.5$  Hz, corresponding to the natural resonant frequency of the linear system without damping. The minimum frequency corresponding to  $\sigma \approx -17$  is  $f_{\min} \approx 0.34$  Hz and the maximum frequency corresponding to  $\sigma \approx +17$  is  $f_{\max} \approx 0.68$  Hz. In this figure, the grey curve corresponds to the primary system with NES without any nonlinear element and two peaks are visible: the highest at 0.51 Hz corresponds to the primary system and the lowest at  $\sqrt{\delta_N} \times 0.51 = 0.36$  Hz corresponds to the linear resonance of the NES. In Figure 6, the thick curves correspond to stable fixed-points, while thin curves correspond to unstable fixed-points. The blue curve is obtained for a nonlinear damping  $\nu_N = 0$ , showing a high amplitude spurious resonance below the natural resonance of the primary system and a small stable detached resonance curve above the natural resonance of the primary system.

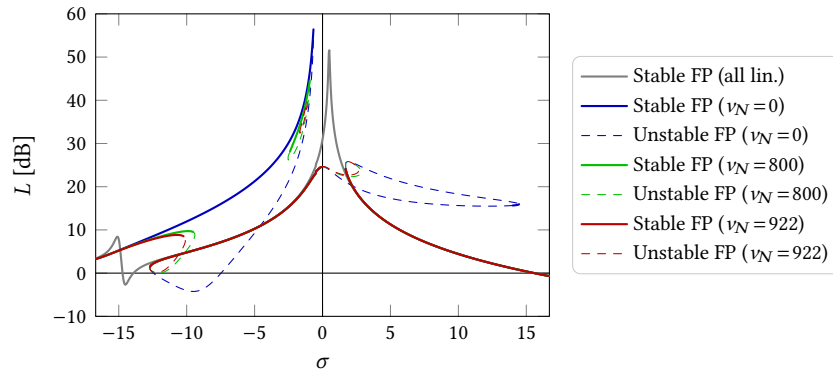


**Figure 6** Stable (thick solid curves) and unstable (thin dashed curves) fixed-points of the primary system for  $A = 10,000 \text{ N}$ ,  $\epsilon = 0.02$ ,  $\mu_N = 0.2$ ,  $\delta_N = 0.5$  and  $K_N = 43$ .

For intermediate values of nonlinear damping, the continuous low-frequency, high-amplitude secondary resonance curve splits into two stable branches, one at low frequency with low amplitude and one at high frequency and amplitude, the latter being the one to be avoided. The green curve, obtained for a nonlinear damping  $\nu_N = 800$ , is an example of this splitting of the detached resonance. In this case, a small detached resonance zone exists around  $\sigma = -1$  and the chosen nonlinear damping is not sufficient to ensure full control of the high amplitude detached resonance. The red curves are obtained for a nonlinear damping  $\nu_N = 922$ , the smallest value that cancels the high amplitude detached resonance curve. It is worth noting that in this case there remains a small detached resonance, but as it is completely unstable it does not pose a problem.

It is worth noting that in this example the frequency range around the main resonance of the primary system is twice as wide as that used in the optimization process to show the influence of low frequency NES resonance and high frequency detached resonance. From a practical point of view, it is sufficient to consider a total frequency range of  $1/3$  octave to estimate the nonlinear damping required to cancel the detached resonance.

The fixed-points on the main curve around the main resonance of the primary system are identical whether linear damping is taken into account or not: the main resonance curves are merged. On the other hand, the introduction of nonlinear damping prevents the emergence of detached resonances without modifying the solution around the resonance of the linear system to be controlled; in the present example, as in all the examples tested, there is only a very slight difference in the calculated level (less than 1 dB) with and without nonlinear damping at the boundaries of the stable zone near the main resonance of the primary system, around  $\sigma = 0$  and  $\sigma = 2$  in Figure 6.

#### 4.2 Slow invariant manifold

A very efficient way to attenuate the vibration is achieved under SMR and is studied under the 1:1 resonance hypothesis (Vakakis et al. 2008, Ch. 6). Two time scales  $\tau_0 = \tau$  and  $\tau_1 = \epsilon\tau$  appear naturally in this type of motion, and a multiple scale asymptotic expansion to order 0 in  $\epsilon$  allows us to obtain this manifold. By introducing perturbation expansion up to order one  $\Phi_i = \phi_i^0 + \epsilon\phi_i^1 + \mathcal{O}(\epsilon^2)$  and by using a multiple-scale asymptotic expansion, we get the following set of differential equations to order 0 in  $\epsilon$ :

$$\phi_1^0 = 0 \tag{13a}$$

$$\phi_2^0 + \frac{1}{2}(\phi_2^0 - \phi_1^0) + \frac{\mu_N \lambda_0}{2} \phi_2^0 - \frac{3i\tilde{K}'_N}{8} |\phi_2|^2 \phi_2 - i\frac{\delta_N}{2} \phi_2^0 = 0 \tag{13b}$$

with  $\tilde{K}'_N = K_N(1 - 2\nu_N\mu_N\lambda_0/(3iK_N))$ . Equation (13a) gives  $\phi_1^0 = \phi_1^0(\tau_1, \tau_2, \dots) = \phi_1$ . The fixed-point  $\phi_2^0 = \phi_2$  of Equation (13b) is solution of

$$i(\phi_2 - \phi_1) + \mu_N \lambda_0 \phi_2 - \frac{3i\tilde{K}'_N}{4} |\phi_2|^2 \phi_2 - i\delta_N \phi_2 = 0. \tag{14}$$

Let us write the fixed-points under polar form  $\phi_1 = \sqrt{Z_1} \exp(i\theta_1)$  and  $\phi_2 = \sqrt{Z_2} \exp(i\theta_2)$ . A few algebraic manipulations lead to the SIM for 1:1 resonance capture

$$Z_1 = \alpha_1 Z_2 + \alpha_2 Z_2^2 + \alpha_3 Z_2^3, \quad (15)$$

where the real coefficients  $\alpha_i$ ,  $i = 1, 2, 3$  are given by

$$\alpha_1 = (\delta_N - 1)^2 + \lambda_0^2 \mu_N^2, \quad (16a)$$

$$\alpha_2 = \frac{3}{2} K_N (\delta_N - 1) + v_N \lambda_0^2 \mu_N^2, \quad (16b)$$

$$\alpha_3 = \frac{1}{16} (9K_N^2 + 4v_N^2 \lambda_0^2 \mu_N^2). \quad (16c)$$

This SIM has one or three solutions. The bifurcation points are obtained by cancelling the derivative of the right hand-side of Equation (15) with respect to  $Z_2$ , that is  $\alpha_1 + 2\alpha_2 Z_2 + 3\alpha_3 Z_2^2 = 0$ . The two roots of this equation are

$$Z_2^{(1)} = \frac{-\alpha_2 - \sqrt{\Delta}}{3\alpha_3} \quad \text{and} \quad Z_2^{(2)} = \frac{-\alpha_2 + \sqrt{\Delta}}{3\alpha_3}. \quad (17)$$

With  $\Delta = \alpha_2^2 - 3\alpha_1\alpha_3$ , one obtains

$$16\Delta = 4(3K_N(\delta_N - 1) + 2v_N \lambda_0^2 \mu_N^2)^2 - 3((\delta_N - 1)^2 + \lambda_0^2 \mu_N^2)(9K_N^2 + 4v_N^2 \lambda_0^2 \mu_N^2). \quad (18)$$

For  $Z_2^{(1,2)}$  to exist,  $\Delta$  must be positive. It is easy to see from Equation (18) that  $\Delta$  is a polynomial of degree 2 in  $\delta_N$ . The values  $\delta_N^{(1,2)}$  cancelling  $\Delta$  are

$$\delta_N^{(1)} = 1 + \sqrt{3} \lambda_0 \mu_N \left( \frac{1}{3} - \frac{4K_N}{3K_N - 2\sqrt{3}v_N \lambda_0 \mu_N} \right), \quad (19a)$$

$$\delta_N^{(2)} = 1 - \sqrt{3} \lambda_0 \mu_N \left( \frac{1}{3} - \frac{4K_N}{3K_N + 2\sqrt{3}v_N \lambda_0 \mu_N} \right). \quad (19b)$$

Two cases should be considered, depending on  $v_N$ :

1.  $v_N = 0$ : Equation (18) becomes  $\Delta = 9K_N^2((\delta_N - 1)^2 - 3\lambda_0^2 \mu_N^2)/4$ . The limit case  $\delta_N = 0$  shows that  $\sqrt{3}\lambda_0 \mu_N < 1$  should hold for the SIM to have at least two bifurcation points. One has

$$\delta_N^{(1)} = 1 - \sqrt{3} \lambda_0 \mu_N, \quad (20a)$$

$$\delta_N^{(2)} = 1 + \sqrt{3} \lambda_0 \mu_N. \quad (20b)$$

We can show that  $\Delta \leq 0$  for  $\delta_N \in [\delta_N^{(1)}, \delta_N^{(2)}]$ , that is  $\Delta \geq 0$  if  $\delta_N \leq \delta_N^{(1)}$  or  $\delta_N \geq \delta_N^{(2)}$ . To ensure  $Z_2^{(1,2)} \geq 0$ , from Equation (17), it is easy to see that since  $\alpha_3 > 0$  irrespective of the values of  $k_N$ ,  $v_N$ ,  $\lambda_0$  and  $\mu_N$ , then  $\alpha_2 < 0$  and, from Equation (16b),  $\delta_N \leq 1$  should hold. We thus recover the classical condition stating that if a NES has a linear stiffness  $\delta_N$ , it must satisfy  $\delta_N < 1 - \sqrt{3}\lambda_0 \mu_N$  (Wu et al. 2021).

2.  $v_N \neq 0$ : it is worth noting that, depending on the considered parameters,  $\delta_N^{(1)}$  is not always smaller than  $\delta_N^{(2)}$ . Let us denote  $v_N^\delta = \sqrt{3}K_N/(2\lambda_0 \mu_N)$  the nonlinear damping that makes  $\delta_N^{(1)}$  singular. In the neighbourhood of  $v_N^\delta$ , with  $v_N = v_N^\delta \pm \eta$ ,  $\eta \ll 1$ , one has

$$\delta_N^{(1)} = 1 + \frac{1}{\sqrt{3}} \lambda_0 \mu_N \pm \frac{2K_N}{\eta} \rightarrow \pm\infty \text{ for } \eta \rightarrow 0, \quad (21a)$$

$$\delta_N^{(2)} = 1 + \frac{1}{\sqrt{3}} \lambda_0 \mu_N \mp \frac{2\lambda_0^2 \mu_N^2 \eta}{3K_N} + O(\eta^2) \rightarrow 1 + \frac{1}{\sqrt{3}} \lambda_0 \mu_N \text{ for } \eta \rightarrow 0. \quad (21b)$$

Depending on the value of  $v_N$  in comparison to  $v_N^\delta$ , two sub-cases should be considered:

- (a)  $v_N > v_N^\delta$ : one has  $\delta_N^{(2)} < \delta_N^{(1)}$  and can show that  $\Delta > 0$  for  $\delta_N \in [\delta_N^{(2)}, \delta_N^{(1)}]$ . Then, for  $Z_2^{(1,2)}$  to exist,  $\delta_N$  must be chosen at least greater than  $\delta_N^{(2)}$ .  $\alpha_2$ , given by Equation (16b), is a strictly increasing function of  $\delta_N$ . Its lowest value is obtained for  $\delta_N^{(2)}$  and is denoted

$$\alpha_2^l = \frac{9K_N\lambda_0\mu_N + 4\lambda_0^3\mu_N^3v_N^2}{2\sqrt{3}K_N + 4\lambda_0\mu_Nv_N} > 0. \quad (22)$$

Since it is positive, none of the bifurcation points  $Z_2^{(1,2)}$  can be positive, and the SIM is a strictly monotone function, which means that no SMR is possible. Then  $v_N$  must not be greater than  $v_N^\delta$ .

- (b)  $v_N < v_N^\delta$ : one has  $\delta_N^{(1)} < \delta_N^{(2)}$  and can show that  $\Delta \leq 0$  for  $\delta_N \in [\delta_N^{(1)}, \delta_N^{(2)}]$ . Accordingly,  $\delta_N$  must be outside the interval  $[\delta_N^{(1)}, \delta_N^{(2)}]$ . Choosing  $\delta_N > \delta_N^{(2)}$  would lead, as shown in Equation (22), to a positive coefficient  $\alpha_2$  which must be avoided. One has to choose  $\delta_N < \delta_N^{(1)}$ . From Equation (19a), it is easy to see that  $\delta_N^{(1)} > 0$  if and only if

$$v_N \leq v_N^m = \frac{3(\sqrt{3}K_N - 3K_N\lambda_0\mu_N)}{2(3\lambda_0\mu_N + \sqrt{3}\lambda_0^2\mu_N^3)} = v_N^\delta \frac{\sqrt{3} - 3\lambda_0\mu_N}{\sqrt{3} + \lambda_0\mu_N}. \quad (23)$$

Since  $\sqrt{3} - 3\lambda_0\mu_N > 0$  implies  $\sqrt{3}\lambda_0\mu_N < 1$ , a negative nonlinear damping is avoided by imposing the condition  $\sqrt{3}\lambda_0\mu_N < 1$ , similar to the condition for the existence of bifurcation points when  $v_N = 0$ . The highest  $\alpha_2$ , denoted  $\alpha_2^h$  and given by Equation (16b), is calculated for  $\delta_N^{(1)}$  and reads

$$\alpha_2^h = -\frac{9K_N\lambda_0\mu_N + 4\lambda_0^3\mu_N^3v_N^2}{2\sqrt{3}K_N - 4\lambda_0\mu_Nv_N}. \quad (24)$$

The denominator  $d_N = 2\sqrt{3}K_N - 4\lambda_0\mu_Nv_N$  becomes  $d_N = 8\sqrt{3}K_N\lambda_0\mu_N/(\sqrt{3} + \lambda_0\mu_N) > 0$  for the maximum admissible value  $v_N^m$ . Then,  $\alpha_2^h \leq 0$  and both bifurcation points  $Z_2^{(1,2)}$  exist. These results can be summarized as follows: if  $v_N \neq 0$ , one must impose  $\sqrt{3}\lambda_0\mu_N < 1$  and  $0 \leq v_N \leq v_N^m$ . In this case it is easy to show that  $\delta_N < \delta_N^{(1)} \in [0, 1 - \sqrt{3}\lambda_0\mu_N]$ .

The stability of the SIM is obtained by a usual linearisation of a complex perturbation about fixed-points of the system composed of Equation (13a) and Equation (13b). Without giving too much detail, this leads to the calculation of roots of the third order characteristic polynomial

$$p(X) = X^3 + \mu_N\lambda_0X^2(1 + Z_2v_N) + \frac{X}{64}((3Z_2K_N + 4\delta_N - 4)(9Z_2K_N + 4\delta_N - 4) + 4\mu_N^2\lambda_0^2(2 + Z_2v_N)(2 + 3Z_2v_N)). \quad (25)$$

If all roots have a real part less than or equal to zero, the SIM is stable. The three roots of this polynomial are

$$X_1 = 0, \quad X_2 = \frac{1}{8}(-4\mu_N\lambda_0(1+v_NZ_2)+\sqrt{\Delta_X}) \quad \text{and} \quad X_3 = \frac{1}{8}(-4\mu_N\lambda_0(1+v_NZ_2)-\sqrt{\Delta_X}) \quad (26)$$

with  $\Delta_X = -48Z_2K_N(-1 + \delta_N) - 16(-1 + \delta_N)^2 + Z_2^2(-27K_N^2 + 4\mu_N^2\lambda_0^2v_N^2)$ . For  $Z_2 \in ]Z_2^{(2)}, Z_2^{(1)}[$ , the SIM is always unstable.

For the parameters  $\epsilon = 0.02$ ,  $\mu_N = 0.2$ ,  $\delta_N = 0.5$  and  $K_N = 43$ , the value of the nonlinear damping that destroys the detached resonance for the maximum system forcing amplitude  $A = 10,000$  N is  $v_N = 922$ . This value is compatible with the constraint given above as  $v_N \leq v_N^m \approx 3,638$ . Note that it is sufficient to cancel the detached resonance for the highest amplitude to ensure that it is cancelled for all lower amplitudes. The SIM is plotted for  $v_N = 0$  and  $v_N = 922$  in Figure 7. In this figure, for any value of nonlinear damping, relaxation oscillations (indicated by green arrows) are observed for which there is a possibility of SMR. The limiting values of  $Z_1$  and  $Z_2$  are given by  $Z_1^* \approx 0.0058$  and  $Z_2^* \approx 0.02$ .

It is worth noting that in Figure 7 the significant nonlinear damping has modified the shape of the SIM in two ways. First, the bifurcation point  $Z_2^{(1)}$  moves away from the abscissa axis, as classically known for a damped system; second, as seen by the shift of the bifurcation points  $Z_2^{(1,2)}$  in the  $(Z_2, Z_1)$  plane, the nonlinear damping slightly reduces the possibility of SMR by shrinking the unstable zone.

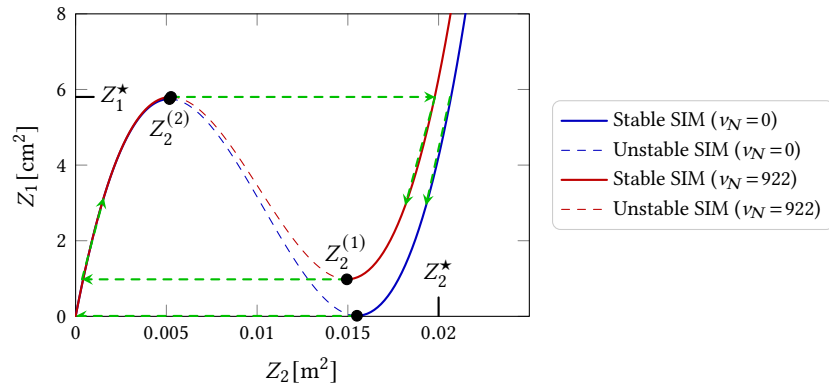


**Figure 7** SIM for  $\epsilon = 0.02$ ,  $\mu_N = 0.2$ ,  $\delta_N = 0.5$  and  $K_N = 43$ .

### 4.3 Numeric simulations compared to analytical results

Two types of comparison are presented in this section. The first is a comparison between the frequency response obtained from a numerical solution of the exact equation (always with 101 frequency points) and that obtained from the analytical solution given in Equations (7a) and (7b). The second one deals with the projection of the numerical time signal onto the SIM given by Equation (15) for two different forcings. The parameters common to all comparisons are  $\epsilon = 0.02$ ,  $\mu_N = 0.2$ ,  $\delta_N = 0.5$  and  $K_N = 43$ .

#### 4.3.1 Numerical simulations compared to analytical results: frequency response function

A comparison between the FRF (i.e. the fixed-points) obtained by integrating the numerical solution of the exact equations and the analytical solution when  $v_N$  is taken to be zero or to the values that cancel the stable detached resonance for a forcing  $A = 9,800$  N is shown in Figure 8. It is worth noting that except for frequencies slightly above the resonance of the linear system (e.g.  $2 < \sigma < 6$ ), where some discrepancies occur, the exact and numerical solutions are very close. If there are two stable branches at a given frequency, the numerical solution may jump from one to the other, depending on the initial conditions. An explanation for the observed discrepancy for frequencies above the resonance of the linear system is given in the next subsection, where it is shown that the solution jumps to another branch of the periodic solution, which is not predicted by the present analysis.

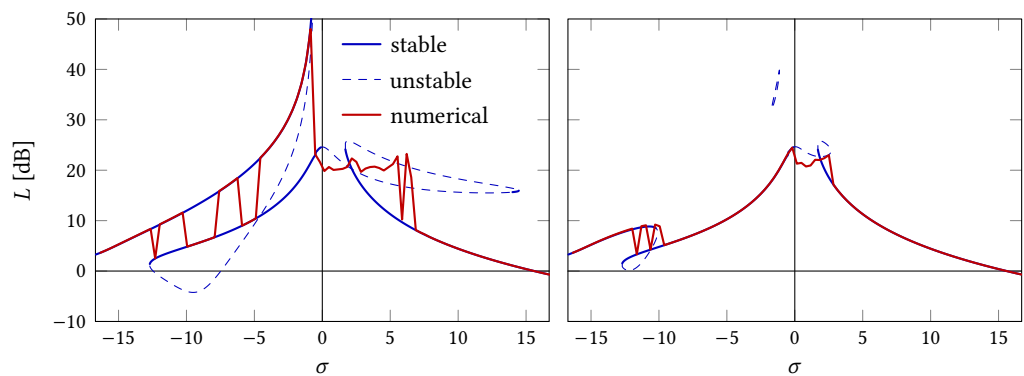


**Figure 8** Fixed-points of the primary system for  $A = 9,800$  N,  $\epsilon = 0.02$ ,  $\mu_N = 0.2$ ,  $\delta_N = 0.5$  and  $K_N = 43$ : stable (solid curves) and unstable (dashed curves) fixed-points. Blue curves correspond to analytical solution. [Left]  $v_N = 0$ . [Right]  $v_N = 922$  for the analytical solution or  $v_N = 822$  for the numerical solution.

#### 4.3.2 Numerical simulations compared to analytical results: time signal projected onto SIM

The second example deals with time motions resulting from the numerical solution of problem equations. In a first example, shown in Figure 9, the forcing had an amplitude of  $A = 9,800$  N and a frequency of  $f = 0.51$  Hz. It is worth noting that in the present case, and for all calculations,

slightly different values of nonlinear damping  $\nu_N$  were required to cancel the detached resonance for numerical and analytical results. The projection of the time series on SIM is given in Figure 10.

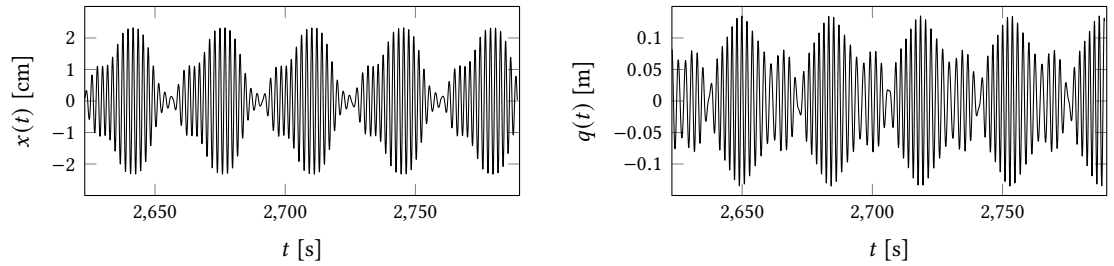


**Figure 9** Time series under SMR for  $A = 9,800$  N,  $f = 0.51$  Hz,  $\epsilon = 0.02$ ,  $\mu_N = 0.2$ ,  $\delta_N = 0.5$ ,  $K_N = 43$  and  $\nu_N = 822$ :  $x(t)$  [Left] and  $q(t)$  [Right].

Amplitude maxima match SIM predictions:  $\max x(t) \approx 0.023$  implies  $(\max x(t))^2 \approx 0.0053 \approx Z_1^*$  and  $\max q(t) \approx 0.135$  implies  $(\max q(t))^2 \approx 0.018 \approx Z_2^*$ . The time series roughly follow the motion predicted by the SIM.

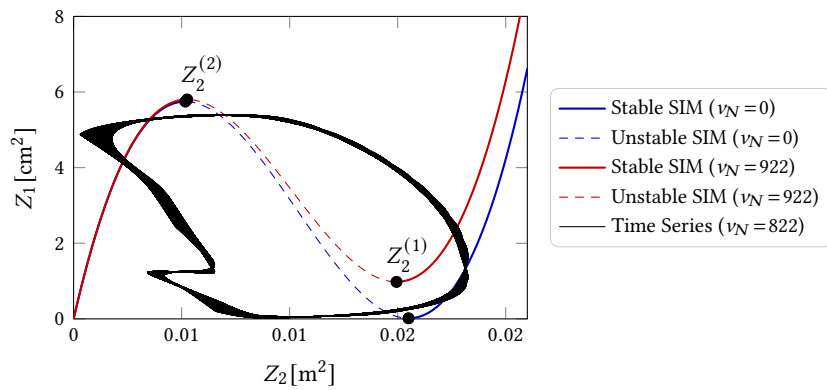


**Figure 10** Projection of time series given in Figure 9 onto SIM for  $A = 9,800$  N,  $f = 0.51$  Hz,  $\epsilon = 0.02$ ,  $\mu_N = 0.2$ ,  $\delta_N = 0.5$ ,  $K_N = 43$  and  $\nu_N = 922$  for analytical calculation or  $\nu_N = 822$  for numerical calculation.

Although these results appear convincing, it must be borne in mind that for different forcing conditions the predictions allowed by SIM under the 1:1 resonance are less relevant. For example, the motion resulting from the numerical solution of the problem equations for a forcing of amplitude  $A = 9,000$  N and frequency  $f = 0.507$  Hz has been plotted in Figure 11.

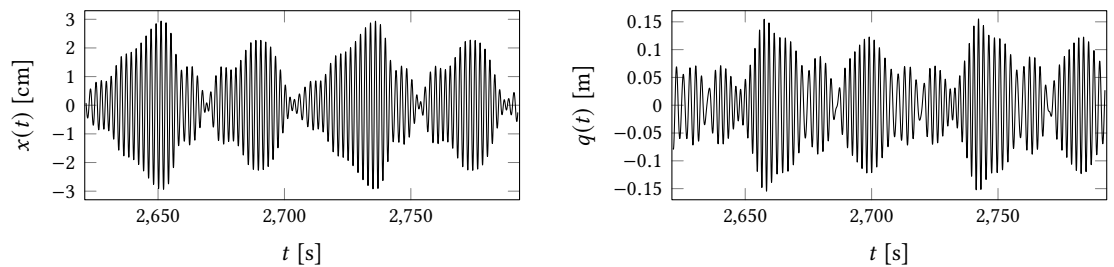


**Figure 11** Time series under SMR for  $A = 9,000$  N,  $f = 0.507$  Hz,  $\epsilon = 0.02$ ,  $\mu_N = 0.2$ ,  $\delta_N = 0.5$ ,  $K_N = 43$  and  $\nu_N = 922$  for analytical calculation or  $\nu_N = 822$  for numerical calculation:  $x(t)$  [Left] and  $q(t)$  [Right].

In this example, SMR shows two different shapes. When the times series is projected onto SIM as shown in Figure 12, it is easy to see that the system partially follows SIM under the 1:1 resonance given in Figure 10 and regularly jumps to another branch of the periodic solution.

To better understand the nature of the transitions that occur, a Hilbert-Huang analysis (see Huang et al. 1998) is performed on the time series. Without going into too much detail about the Hilbert-Huang transform (HHT), the core of this method is to decompose the signal into what's called empirical modes, hence the name *Empirical mode decomposition* (EMD). Based on these signal modes, the so-called *Intrinsic mode function* (IMF), the signal is split into decreasing

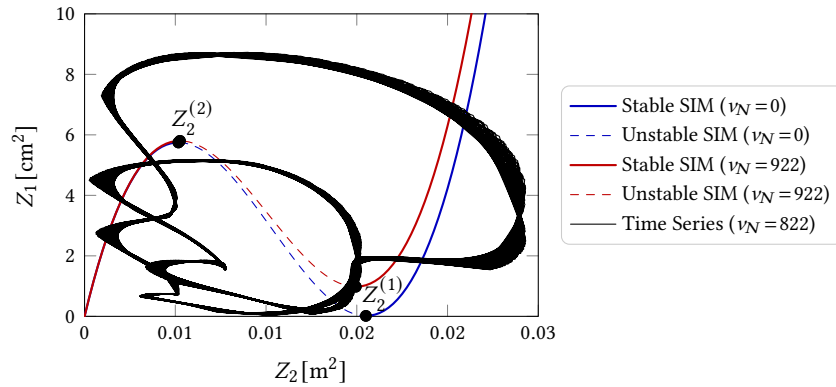


**Figure 12** Projection of time series given in Figure 11 onto SIM for  $A = 9,000$  N,  $f = 0.507$  Hz,  $\epsilon = 0.02$ ,  $\mu_N = 0.2$ ,  $\delta_N = 0.5$ ,  $K_N = 43$  and  $\nu_N = 922$  for analytical calculation or  $\nu_N = 822$  for numerical calculation.

frequency components, each of which has only one frequency component at a time; then a Hilbert spectral analysis (HSA) is performed, which allows the instantaneous frequency of each IMF to be calculated. In general, a signal has less than 10 IMFs, but 20 IMFs are possible for particularly rich signals.

One of the main difficulties of this method is the extraction of the IMFs, and the program proposed by Loudet (2009) (a simple executable code running under Windows) allows fast and efficient EMD. For the time series given in Figures 9 and 11, less than 6 IMFs were needed to analyze the signals and only the first three contain significant data. The results of the HHT analysis of the time series in Figure 9 are indicated in Figure 13. The results of the HHT analysis of the time series in Figure 11 are indicated in Figure 14. In each of these figures three sub-figures are given, the top one is the corresponding IMF, the middle coloured figure is the wavelet analysis of the IMF and the bottom one is the instantaneous frequency obtained by HSA. It is worth noting that the instantaneous frequency curves have been plotted using the convention that the higher the IMF amplitude, the darker the curve.

For regular SMR, corresponding to the time series in Figure 9, the HHT of the linear system in Figure 13 shows that the motion during SMR occurs at the forcing frequency and no significant energy conversion is observed; the first IMF contains most of the energy of the linear system motion. At the transition between two bursts, motion occurs with small amplitude (the amplitude of IMF<sub>2</sub> is by a factor 100 smaller than that of IMF<sub>1</sub>) and with a frequency mainly  $f_0/3$  and with an even smaller component at IMF<sub>3</sub> (one third of IMF<sub>2</sub>) with a frequency  $f_0/5$ . The HHT of the NES motion in Figure 13 shows a similar behaviour with an obvious significant frequency variation for the NES and an amplitude of the second IMF only ten times smaller than the first with a frequency mainly at  $f_0/3$ . This indicates a 1:1 resonance capture during the SMR and a 1:3 resonance capture during the transition between two bursts.

For the double SMR, corresponding to the time series in Figure 11, the HHT of the linear system in Figure 14 shows that the energy during the two types of SMR is located at the forcing frequency and no significant energy conversion is observed; the first IMF contains most of the linear system motion energy. At the transition between two bursts, motion of small amplitude (the amplitude of IMF<sub>2</sub> is about one hundred less than that of IMF<sub>1</sub>) occurred with a frequency mainly  $f_0/2$  and with an even smaller component at IMF<sub>3</sub> (one third of IMF<sub>2</sub>) with a frequency  $f_0/5$ . The HHT of the NES motion in Figure 14 shows a similar behaviour with an apparent significant frequency variation for the NES, an amplitude of the second IMF only ten times smaller than the first IMF with a frequency mainly at  $f_0/3$ . This indicates a 1:1 resonance capture during the SMR and a 1:2 resonance capture for the linear system and a 1:3 resonance capture for the NES during the transition between two bursts. This could correspond to a transient instability leading to 1:3 resonance capture observed by Andersen et al. (2012) with a lower amplitude pulse than that ensuring 1:1 resonance capture at high amplitude pulse. Obviously the systems studied differ by the forcing, impulse for Andersen et al. (2012) and continuous forcing in the present work. However, as noted by Andersen et al. (2012), *this instability is attributed solely to passive nonlinear damping*. While further analytical studies would have been useful, this is not the core

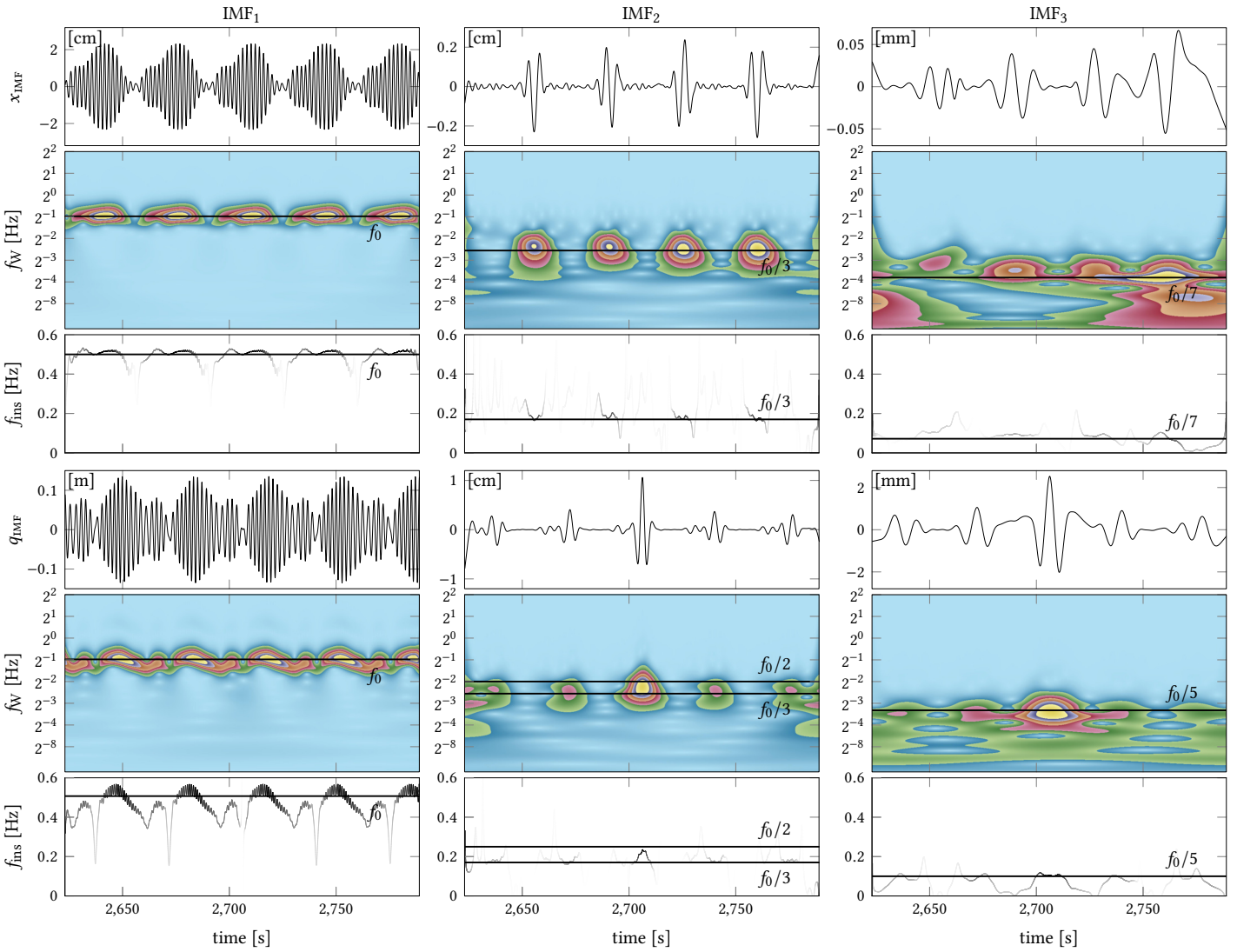


**Figure 13** IMFs of  $x(t)$  [top] and  $q(t)$  [bottom] with corresponding frequency  $f_W(t)$  through Wavelet transform and instantaneous frequency  $f_{int}(t)$  through HHT. Units of IMF time series indicated at the top left corner of the corresponding plot.  $A = 9,800$  N,  $f = 0.510$  Hz,  $\epsilon = 0.02$ ,  $\mu_N = 0.2$ ,  $\delta_N = 0.5$ ,  $K_N = 43$  and  $\nu_N = 822$ .

of this work and is left for future work.

All these results clearly show that the consideration of nonlinear damping, while changing the behaviour of the system by removing the detached resonances, does not fundamentally change the nature of the coupling between the primary system and the NES.

## 5 Optimization results

We proceeded to minimize the function  $J$ , defined in Equation (4), of more than a hundred different configurations, obtained by fixing  $\epsilon$  and  $\mu_N$  for  $\epsilon \in [0.001, 0.05]$  and  $\mu_N \in [0.1, 1]$ , and looking for values of  $\delta_N$  and  $K_N$  that allowed the greatest average attenuation over the whole range of wind turbine forcing. Once these estimates have been made, and this is the most computationally intensive part of the work as each configuration takes about three days of parallel computation, one looks for the smallest value of  $\nu_N$  that avoids the phenomenon of detached resonance; such an estimate is easy to make as the analytical result gives an accurate estimate of the actual value.

Although not all the details are given here, it is worth noting that, particularly for small values of  $\epsilon$ , multiple combinations (2 or 3) of  $K_N$  and  $\delta_N$  give comparable values of damping. Since in this case it is very difficult to estimate an absolute minimum, we decided to choose identified values that, as far as possible, ensure a regular evolution with respect to  $\epsilon$  and  $\mu_N$ .



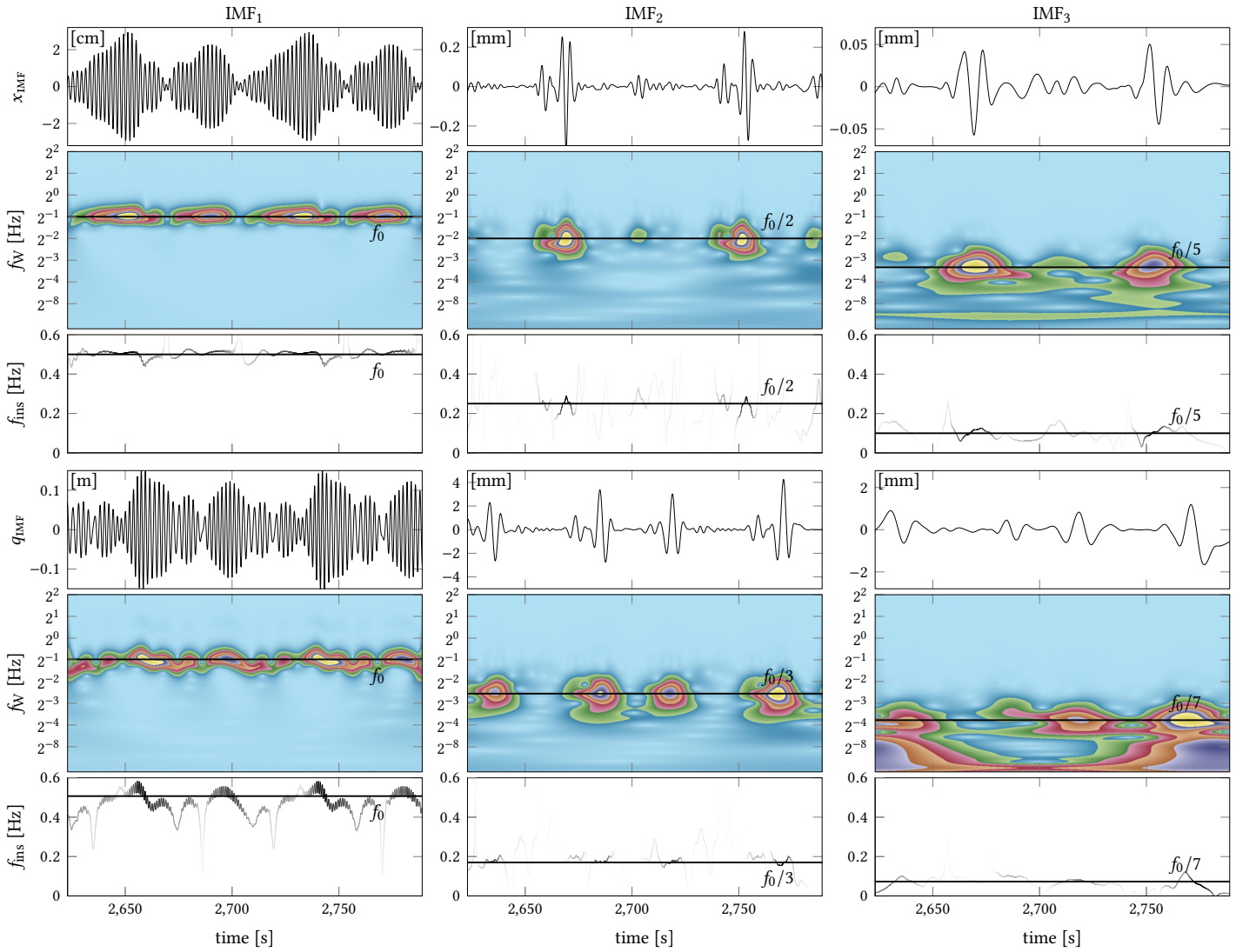


**Figure 14** IMFs of  $x(t)$  [top] and  $q(t)$  [bottom] with corresponding frequency  $f_W(t)$  through Wavelet transform and instantaneous frequency  $f_{int}(t)$  through HHT. Units of IMF time series indicated at the top left corner of the corresponding plot.  $A = 9,000$  N,  $f = 0.507$  Hz,  $\epsilon = 0.02$ ,  $\mu_N = 0.2$ ,  $\delta_N = 0.5$ ,  $K_N = 43$  and  $\nu_N = 822$ .

An example of multiple minima of  $J$ , as defined in Equation (4), is illustrated in Figure 15. It

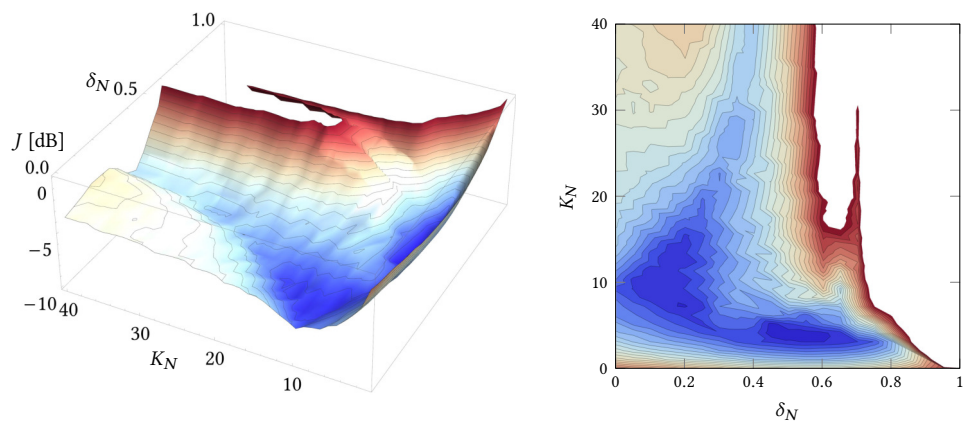


**Figure 15** Map of  $J$  as a function of  $\delta_N$  and  $K_N$  for  $\epsilon = 0.004$  and  $\mu_N = 0.3$ . Left: 3-D plot, right: contour plot.

shows a 3D plot and a contour plot of  $20 \log |J|$  versus  $\delta_N \in [0; 1]$  and  $K_N \in [0; 40]$  for  $\epsilon = 0.004$  and  $\mu_N = 0.3$ . In this figure, only negative values of  $J$  are plotted, corresponding to a reduction in the oscillation of the primary system. This shows that there are two separate minima, the first near  $\delta_N \approx 0.5$ ,  $K_N \approx 5$  and the second near  $\delta_N \approx 0.2$ ,  $K_N \approx 8$ . A refined study around these two

points yields

$$\delta_N = 0.48, \quad K_N = 5.4 \quad \Rightarrow \quad J = -8 \text{ dB} \tag{27a}$$

$$\delta_N = 0.19, \quad K_N = 8.1 \quad \Rightarrow \quad J = -7.7 \text{ dB}. \tag{27b}$$

Although comparable, the minimum in Equation (27a) gives a slightly better damping and a smoother variation of  $\delta_N$  and  $K_N$  when  $\epsilon$  and  $\mu_N$  vary. It is then selected. It is worth noting that for a significant range of  $\delta_N$  and  $K_N$ , in white in Figure 15, the choice of parameters leads to a positive  $J$ , meaning an increase in the response of the linear system, which must be avoided at all costs. As we have seen, the linear stiffness must satisfy  $\delta_N < 1 - \sqrt{3}\lambda_0\mu_N$ , and in the present case, with  $\lambda_0 = 0.25$  and  $\mu_N = 0.3$ , one must have  $\delta_N < 0.9$ . This limit is observed in the right sub-figure in Figure 15, where whatever  $K_N$ , if  $\delta_N > 0.9$  then  $J > 0$  and the chosen parameters lead to an NES that is unable to reduce the vibration of the primary linear system.

The results are shown in Figure 16 for  $\delta_N$  (left) and  $K_N$  (right); in this figure,  $\delta_N$  and  $K_N$  are plotted versus  $\epsilon$  which give the best damping imposing zero initial conditions for different NES linear damping  $\mu_N$ . It is obvious that for small values of  $\epsilon$  (say, less than 0.5 %) both  $\delta_N$  and  $K_N$  show significant variations, while for  $\epsilon > 1\%$  they become smoother and more regular. For sufficiently high values of  $\epsilon$ , both parameters show a power dependence with respect to  $\epsilon$  and  $\mu_N$ ; while not completely clear for  $\delta_N$ , it is obvious for  $K_N$ . This will be clarified later.

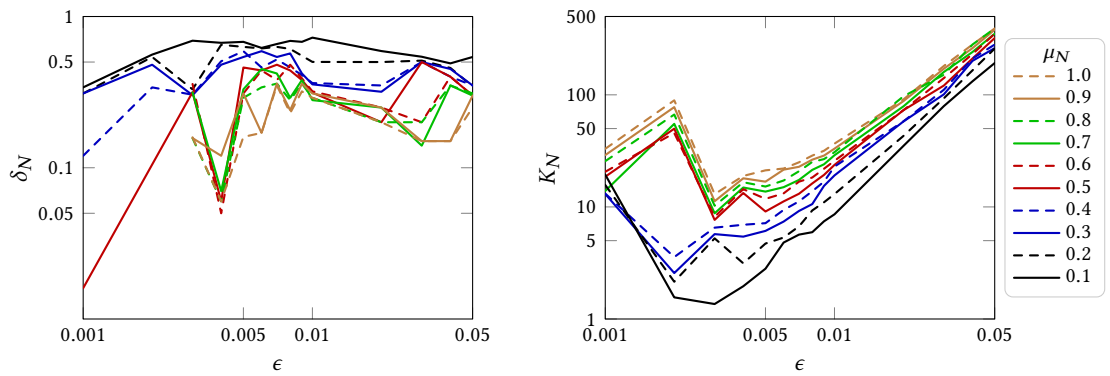


**Figure 16** Identified optimal parameter in terms of  $\epsilon$  for various linear damping  $\mu_N$ . [Left]  $\delta_N$ , [Right]  $K_N$ .

In order to ensure that the solutions bifurcate to the detached resonance, non-zero initial conditions are imposed and the values of the nonlinear damping that cancel it out for the largest forcing  $A_{\max}$  are given in Figure 17. Results are shown for the analytical approximate solution

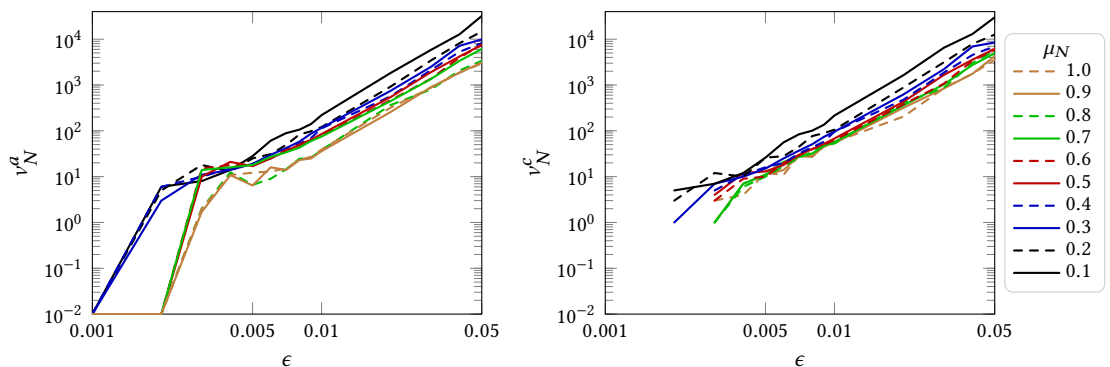


**Figure 17** Identified optimal nonlinear damping in terms of  $\epsilon$  for various linear damping  $\mu_N$ . [Left] analytical  $v_N^a$ , [Right] numerical  $v_N^c$ .

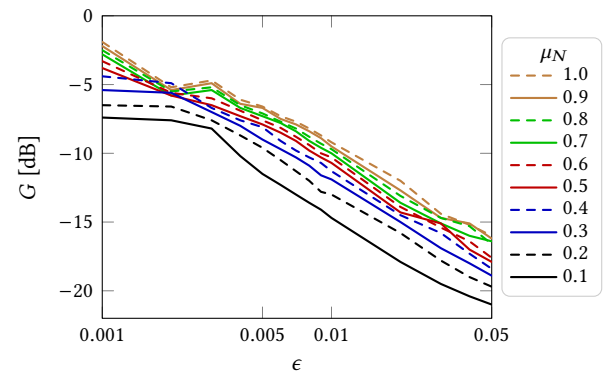
(left) denoted  $v_N^a$  and for the numerical simulation of the exact solution (right) denoted  $v_N^c$ . Again, it is clear that for small values of  $\epsilon$  (say less than 0.5 %), the nonlinear damping obtained both from analytical  $v_N^a$  and numerical  $v_N^c$  estimates show significant variations, while for  $\epsilon > 1\%$ , they become smoother and more regular with comparable numerical values. Without going into too much detail, these variations are observed when the function to be minimized,  $J$ , has more

than one minimum and when one of these minima vanishes or appears when  $\epsilon$  varies. It should be noted that for very low  $\epsilon$  (less than 0.2 %) there is no clear detached resonance and nonlinear damping is useless; however, in this case, the NES does not allow efficient vibration control of the primary linear system (only a few dB) and, combined with high variation of the identified coefficients, the solution with very small  $\epsilon$  cannot be considered as efficient.

As observed for  $\delta_N$  and  $K_N$ , both parameters  $v_N^a$  and  $v_N^c$  exhibit a power dependence with respect to  $\epsilon$  and  $\mu_N$ . For the highest values of  $\epsilon$ , the analytical and numerical nonlinear dampings show significantly high values. However, it should be noted that the damping of the NES is  $\epsilon\mu_N\lambda_0(1 + 2v_N w^2(t))\dot{w}(t)$  with  $\lambda_0 = 0.1$  for  $\epsilon = 0.01$  and  $\mu_N \in [0.1, 1]$ . In fact, even if the values of  $v_N$  seem high, the values of  $\epsilon\mu_N\lambda_0v_N$  remain in acceptable orders of magnitude. To confirm this, let us define a NES mass  $m_N = \epsilon m_0 = 10,000$  kg and  $\mu_N = 0.5$ . With  $\epsilon = 0.01$ , we have  $\lambda_0 = c_0/(m_N\omega_0) \approx 0.1$ , the optimal values of  $v_N$  are 68 for the numerical solution of the exact equation and 85 for the analytical solution; accordingly, we take  $v_N \approx 80$ . For  $\mu_N = 0.5$ , i.e. a linear NES damping of half that of the primary system, we have  $c_N = 1,600$  N s/m. The nonlinear damping coefficient is then  $2v_Nc_N \approx 260,000$  N s/m, which for a linear frequency of 0.5 Hz, corresponds to an approximate linear damping  $\zeta_N = 2v_Nc_N/(2m_N\omega_0) \approx 4$ .

Finally, Figure 18 shows the best average gain obtained as a function of mass  $\epsilon$  and damping  $\mu_N$ .  $G$  represents the mean level of the RMS value for the linear system, normalized to the mean

**Figure 18** Best average gain obtained for various NES linear dampings.



level of the RMS value for the linear system without nonlinear dependence in stiffness and damping; the value is calculated over the whole amplitude range  $A \in [0, 10,000]$  N. The best reduction (up to 21 dB mean average reduction) is obtained for the NES with the highest mass and lowest damping. Again, the attenuation becomes smoother and more regular for  $\epsilon > 1\%$ .

All these regular curves in logarithmic plots suggest, except for the lowest values of  $\epsilon$ , a dependence of the parameters as a function of the powers of  $\epsilon$  and  $\mu_N$ . The identification performed on the whole data set leads to the following results:

$$G_{\text{dB}} \approx C_G \epsilon^{1/3} \mu_N^{-1/6}, \quad C_G \approx -43.1 \quad (28a)$$

$$K_N \approx C_K \epsilon^{3/2} \mu_N^{1/3}, \quad C_K \approx 35,150 \quad (28b)$$

$$v_N^a \approx v_N^c \approx C_v \epsilon^3 \mu_N^{-1}, \quad C_v \approx 2.5 \times 10^7 \quad (28c)$$

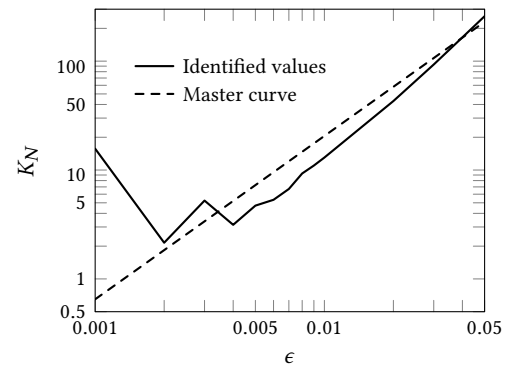
$$\delta_N \approx C_\delta (1 + \alpha_1 \epsilon + \alpha_2 \epsilon^2) (1 + \beta_1 \mu_N + \beta_2 \mu_N^2) \quad (28d)$$

with, for  $0.001 \leq \epsilon < 0.009$ ,  $C_\delta \approx 0.063$ ,  $\alpha_1 \approx 3329.5$ ,  $\alpha_2 \approx -228,301$ ,  $\beta_1 \approx -1.2$  and  $\beta_2 \approx 0.47$  and for  $0.009 \leq \epsilon \leq 0.05$ ,  $C_\delta \approx 0.77$ ,  $\alpha_1 \approx -11.5$ ,  $\alpha_2 \approx 144.11$ ,  $\beta_1 \approx -1.3$  and  $\beta_2 \approx 0.65$ .

The values obtained for optimal nonlinear damping are almost identical for the analytical and numerical solutions and can be described by the same power law. This is an indication that the analytical approximation obtained under the 1:1 resonance assumption is sufficient to describe the cancellation of detached resonances by nonlinear damping.

A comparison between a master curve and the identified  $K_N$  vs  $\epsilon$  for  $\mu_N = 0.2$  is indicated in Figure 19. Except for the lowest  $\epsilon$ , where the strongest fluctuations are observed, the results are satisfactory and at least sufficient to give an initial value for more refined calculations.

**Figure 19** Comparison of a master curve and the identified values for  $K_N$  vs  $\epsilon$  for  $\mu_N = 0.2$ .



## 6 Conclusion

This work was dedicated to the vibration mitigation of a simplified model of a FOWT by a NES with both linear and nonlinear stiffness and damping. It has been shown that the tuning of the nonlinear viscous damping of the NES allows the complete elimination of detached resonances and maintains the nonlinear absorber capacity to strongly limit the vibrations of the wind turbine over its entire operating range.

Furthermore, it has been shown that classical nonlinear dynamics tools (fixed-points, SIM) can easily take into account this type of nonlinear damping and perform fast analytical studies. It has been shown that most of the system dynamics are conserved when nonlinear damping is added to the system. In particular, the fixed-points of the main FRF are slightly modified when nonlinear damping is added to destroy detached resonances. Most of the influence of nonlinear damping was observed on the SIM, the shape of which remains largely unchanged when nonlinear damping is considered. Using the SIM properties, an upper bound for nonlinear damping that allows SMR has been proposed.

Using a two-step optimization procedure, it has been shown how to define parameters that strongly limit the vibration of a simplified model of the FOWT over its entire excitation range and over a significant frequency range. The first step consists in imposing a zero initial condition and optimizing the linear and cubic stiffness for different NES masses and linear damping by minimizing the FOWT ridge curve over its entire excitation range. The second step, after calculating the optimal parameters, is to estimate the nonlinear damping of the NES that cancels the detached resonance for the maximum amplitude.


The parametric study shows that the parameters, such as linear and nonlinear stiffnesses, attenuation and nonlinear damping, depend on simple power laws in the NES mass and linear damping. This simple result is sufficient for NES design, or at least, can be used as an estimate for a more refined optimization process.

## References

- Abramson, H. N. (1955). Response curves for a system with softening restoring force. *Journal of Applied Mechanics* 22(3):434–435. [DOI].
- AL-Shudeifat, M. (2014). Highly efficient nonlinear energy sinks. *Nonlinear Dynamics* 76(4):1905–1920. [DOI], [HAL].
- Alexander, N. and F. Schilder (2009). Exploring the performance of a nonlinear tuned mass damper. *Journal of Sound and Vibration* 319(1-2):445–462. [DOI], [HAL].
- Andersen, D., Y. Starosvetsky, A. Vakakis, and L. Bergman (2012). Dynamic instabilities in coupled oscillators induced by geometrically nonlinear damping. *Nonlinear Dynamics* 67(1):807–827. [DOI], [HAL].
- Bakre, S. V. and R. S. Jangid (2007). Optimum parameters of tuned mass damper for damped main system. *Structural Control and Health Monitoring* 14(3):448–470. [DOI], [HAL].
- Bellet, R., B. Cochelin, P. Herzog, and P.-O. Mattei (2010). Experimental study of targeted energy transfer from an acoustic system to a nonlinear membrane absorber. *Journal of Sound and Vibration* 329(14):2768–2791. [DOI], [HAL].

- Chen, Y.-Y., Z.-C. Qian, W. Zhao, and C.-M. Chang (2020). A magnetic bi-stable nonlinear energy sink for structural seismic control. *Journal of Sound and Vibration* 473:115233–1–17. [DOI].
- Den Hartog, J. (1947). *Mechanical Vibrations*. 3rd ed. McGraw-Hill Book Company.
- Ding, H. and L.-Q. Chen (2020). Designs, analysis, and applications of nonlinear energy sinks. *Nonlinear Dynamics* 100(4):3061–3107. [DOI], [HAL].
- Gendelman, O., L. Manevitch, A. Vakakis, and R. M’Closkey (2001). Energy pumping in nonlinear mechanical oscillators: Part I—Dynamics of the underlying Hamiltonian systems. *Journal of Applied Mechanics* 68(1):34–41. [DOI], [HAL].
- Gendelman, O., T. Sapsis, A. Vakakis, and L. Bergman (2011). Enhanced passive targeted energy transfer in strongly nonlinear mechanical oscillators. *Journal of Sound and Vibration* 330(1):1–8. [DOI], [HAL].
- Gourc, E., G. Michon, S. Seguy, and A. Berlioz (2014). Experimental investigation and design optimization of targeted energy transfer under periodic forcing. *Journal of Vibration and Acoustics* 136(2):1–8. [DOI], [HAL].
- Gourc, E., G. Michon, S. Seguy, and A. Berlioz (2015). Targeted energy transfer under harmonic forcing with a vibro-impact nonlinear energy sink: Analytical and experimental developments. *Journal of Vibration and Acoustics* 137(3):031008. [DOI], [HAL].
- Habib, G., G. Cirillo, and G. Kerschen (2018). Isolated resonances and nonlinear damping. *Nonlinear Dynamics* 93(3):979–994. [DOI], [ARXIV].
- Habib, G. and F. Romeo (2020). Comparative analysis of NES and TMD performance via high-dimensional invariant manifolds. *IUTAM Symposium on Exploiting Nonlinear Dynamics for Engineering Systems* (Novi Sad, Serbia, July 15–19, 2018). Springer, pp 143–153. [DOI], [HAL].
- Huang, N., Z. Shen, S. Long, M. Wu, H. Shih, Q. Zheng, N.-C. Yen, C. C. Tung, and H. Liu (1998). The empirical mode decomposition and the Hilbert spectrum for nonlinear and non-stationary time series analysis. *Proceedings of the Royal Society of London. Series A: Mathematical, Physical and Engineering Sciences* 454(1971):903–995. [DOI], [HAL].
- Liu, Y., A. Mojahed, L. Bergman, and A. Vakakis (2019). A new way to introduce geometrically nonlinear stiffness and damping with an application to vibration suppression. *Nonlinear Dynamics* 96(3):1819–1845. [DOI].
- Loudet, L. (2009). *Application of Empirical Mode Decomposition to the detection of sudden ionospheric disturbances by monitoring the signal of a distant very low frequency transmitter*. Version 1. [URL].
- Pahn, T., J. Jonkman, R. Rolfes, and A. Robertson (2012). Inverse load calculation of wind turbine support structures - A numerical verification using the comprehensive simulation code FAST. *53rd AIAA/ASME/ASCE/AHS/ASC Structures, Structural Dynamics and Materials Conference* (Honolulu, Hawaii, Apr. 23–26, 2012). AIAA. [DOI], [OA].
- Rauscher, M. (1938). Steady oscillations of systems with nonlinear and unsymmetrical elasticity. *Journal of Applied Mechanics* 5(4):A169–A177. [DOI], [OA].
- Starosvetsky, Y. and O. Gendelman (2008). Attractors of harmonically forced linear oscillator with attached nonlinear energy sink. II: Optimization of a nonlinear vibration absorber. *Nonlinear Dynamics* 51(1-2):47–57. [DOI], [HAL].
- Starosvetsky, Y. and O. Gendelman (2009). Vibration absorption in systems with a nonlinear energy sink: Nonlinear damping. *Journal of Sound and Vibration* 324(3-5):916–939. [DOI], [HAL].
- Vakakis, A., O. Gendelman, L. Bergman, M. McFarland, G. Kerschen, and Y. S. Lee (2008). *Nonlinear Targeted Energy Transfer in Mechanical and Structural Systems*. Springer. [DOI].
- Wang, J., N. Wierschem, B. Spencer, and X. Lu (2015). Track nonlinear energy sink for rapid response reduction in building structures. *Journal of Engineering Mechanics* 141(1):04014104–1–10. [DOI].
- Wolfram Research, Inc. (2021). *Mathematica 13.0*. Version 13. [URL].
- Wu, Z., S. Seguy, and M. Paredes (2021). Basic constraints for design optimization of cubic and bistable nonlinear energy sink. *Journal of Vibration and Acoustics* 144(2). [DOI], [HAL].
- Zuo, H., K. Bi, and H. Hao (2020). A state-of-the-art review on the vibration mitigation of wind turbines. *Renewable and Sustainable Energy Reviews* 121:109710. [DOI].
- Zuo, H. and S. Zhu (2022). Development of novel track nonlinear energy sinks for seismic

performance improvement of offshore wind turbine towers. *Mechanical Systems and Signal Processing* 172:108975. [DOI].

**Open Access** This article is licensed under a Creative Commons Attribution 4.0 International License, which permits use, sharing, adaptation, distribution and reproduction in any medium or format, as long as you give appropriate credit to the original author(s) and the source, provide a link to the Creative Commons license, and indicate if changes were made. The images or other third party material in this article are included in the article's Creative Commons license, unless indicated otherwise in a credit line to the material. If material is not included in the article's Creative Commons license and your intended use is not permitted by statutory regulation or exceeds the permitted use, you will need to obtain permission directly from the authors—the copyright holder. To view a copy of this license, visit [creativecommons.org/licenses/by/4.0](https://creativecommons.org/licenses/by/4.0). 

**Authors' contributions** R.C. and P.-O.M. developed the methodology and wrote the paper, P.-O.M. wrote the code and performed the computations.

**Supplementary Material** None.

**Acknowledgements** The authors would like to thank Etienne GOURC for their careful reading of the text.

**Ethics approval and consent to participate** Not applicable.

**Consent for publication** Not applicable.

**Competing interests** The authors declare that they have no competing interests.

**Journal's Note** JTCAM remains neutral with regard to the content of the publication and institutional affiliations.